Thermal conductance enhanced via inelastic phonon transport by atomic vacancies at Cu/Si interfaces

Zexi Lu, Anne M. Chaka,* and Peter V. Sushko
Pacific Northwest National Laboratory, Richland, Washington 99352, USA

(Received 9 April 2020; revised 13 July 2020; accepted 17 August 2020; published 31 August 2020)

Understanding and controlling heat transfer across interfaces has become an important issue for the performance of micro- and nanoscale electronics, as well as achieving a high figure of merit for thermoelectrics. Intrinsic and extrinsic defects can have a significant impact on thermal transport in bulk materials and across interfaces, but the mechanism is not well understood. In this work, nonequilibrium molecular dynamics simulations are used to determine the impact of interfacial atomic vacancies on thermal transport across a Cu/Si junction. In contrast to the reduction in thermal transport typically seen with bulk defects, we find that by introducing atomic vacancies at a concentration of 6.3% near the interface in either or both materials, the interfacial thermal conductance can be increased by up to 76%. By controlling the initial positions of the vacancies and keeping track of their movements and population, we find that interfacial thermal transport is dependent on temperature, vacancy concentration, and distribution, and a positive correlation between the conductance and point defect activities (extent of vacancy migration, rate of Frenkel defect creation and annihilation) is observed. Further calculations based on the phonon density of states and normal mode decomposition reveal that the increase in interfacial thermal conductance originates primarily from high-frequency phonons, supported by enhanced inelastic phonon transport which contributes to more than 60% of the increase. Our findings suggest a practical way to manipulate inelastic phonon conversion through the presence of defects, which provides an alternative perspective on improving thermal transport between materials with a large lattice mismatch.

DOI: 10.1103/PhysRevB.102.075449

I. INTRODUCTION

The drive to make electronic devices as small and as dense as possible has introduced challenges in thermal management [1,2]. Enhancing heat dissipation has become critically important for the function and performance of micro- and nanoelectronics [3], whereas thermal insulation is essential for achieving a high figure of merit for nanoscale thermoelectrics [4,5]. At the nanoscale where the surface-to-volume ratio is high, the microstructure of interfaces can dominate thermal transport more than the properties of the bulk materials [6–9]. Hence understanding how structural and chemical inhomogeneities at the atomic level affect heat transfer across interfaces is essential in the design of new materials and devices. Although good progress has been made towards understanding mechanisms of heat transfer across a wide range of simple crystalline materials from metals to semiconductors to ionic salts [10,11], significant challenges arise at interfaces due to the complex scattering of phonons. Determining the factors that impact heat transfer across interfaces is complicated by the difficulties in experimental characterization of buried interfaces [12], control of defects, and separation of bulk from interface effects, as well as challenges in measurement of nanoscale heat transfer such as determining the contact area from asperities during mechanical contact or the impact of grease [13–15]. Hence, atomistic simulations that provide detailed insight into the effects of interfacial structure, composition, and defects can play a key role in delineating the factors affecting heat transfer and optimizing design of materials and devices [16–18].

Much of the computational work to date has been performed on clean, defect-free interfaces between materials with lattice-matched heteroepitaxy such as Si/Ge [19–21], GaAs/AlAs [22], and Ar/heavy-Ar [23]. These systems enabled study of fundamental properties of phonon transport without strain, which in general has found that interfacial thermal conductance increases with increased interfacial bonding strength [24–26], temperature [19,21], overlap of phonon density of states (PDOS) [19,27], and inelastic scattering [21,23]. Recent simulations and experimental work representing more realistic materials with mismatched lattices [28], disorder [29], and rough interfaces [30–33], however, indicated that phonon transport was more complex than simple trends would suggest. Overlap of PDOS is not always predictive [34], and roughness or disorder can either increase [28,33,35–37] or decrease [30–32,38–40] interfacial thermal transport depending upon structural details.

The impact of defects on thermal transport is even less understood, though they occur in virtually all materials. Experimental work has been limited, but underscores that the impact of defects on thermal transport is significant [41]. Early studies by Walker and others in 1963 indicated that point defects introduced new phonon modes in both optical and acoustic branches that could not be explained by simple Rayleigh scattering [42]. This impact has also been observed across a

*anne.chaka@pnnl.gov

wide range of systems from two-dimensional graphene [43], graphene/BN interfaces [44,45], and MoS_2 layered systems [46], to Al/Si interfaces with roughness and oxidation layers [47], and to ion implanted Si and amorphous SiOC:H/SiC:H interfaces [48,49]. In general, shorter-wavelength phonons are more sensitive to the presence of defects than longer wavelengths, and the presence of defects reduces thermal conductivity. For the ion implantation experiments, however, Scott *et al.* determined that point defects from Si cation ion implantation in Si decreased thermal conductivity, particularly if the local induced strain was high [48], whereas Gorham *et al.* [50] observed that proton irradiation increased thermal conductance across an Al/native oxide/Si interface, likely due to the ion beam causing increased interfacial mixing. Hence the impact of the defects depends on many factors, including the type of defects and their distribution in the material.

Given the range of structures and variations in experimental results for the impact of defects on interfacial thermal conductance, systematic computational investigations are particularly valuable to gain insight into the underlying lattice vibration-defect coupling mechanisms. In 1955 Klemens performed foundational theoretical work on a simple cubic lattice to determine the frequency dependence of elastic scattering of phonons by lattice points, dislocations, and grain boundaries [51]. Additional investigations on bulk dislocations [28], grain boundaries [52–54], and vacancies [43,55] indicated that there was a dependence on mode and frequency for how phonons interact with defects, but with considerable variation from system to system and the type of defect. Despite this progress on bulk defects, detailed understanding of the impact of defects on interfacial thermal transport, and their relationships with the underlying phonon-defect scattering mechanisms, is still lacking.

In this study, we focus on one type of point defect, vacancies at the interface, to identify their relationship with interfacial thermal transport. Cu/Si interfaces are chosen as they are representative of realistic junctions with wide technological applications. Vacancies are arranged systematically across a range of concentrations, distributions, and locations at or near the interface in either or both materials. We utilize classical nonequilibrium molecular dynamics (NEMD) simulations to calculate the Kapitza resistance across the interface at 150 and 350 K, as it is a powerful technique to understand thermal transport integrated over all vibrations [56]. NEMD intrinsically includes all the phonon scattering mechanisms, both elastic and inelastic, and predicts reasonable thermal properties with well-developed interatomic potentials. The classical phonon occupation in NEMD deviates from quantum-mechanical theory, but can still provide reasonable predictions which can be further refined by corrections [57]. A deeper understanding of phonon-defect scattering mechanisms, however, requires deconvolution to determine phonon transport as a function of frequency. Hence spectral analysis is employed to delineate the impact of temperature, vacancy distribution, and frequency on the transport of phonons across the interface. It should be noted that we are considering thermal transport due to phonons only, and not electrons as their thermal conductivity in pure Si is negligible. While Cu electrons participate in interfacial thermal transport through electron-phonon coupling [58,59], there is no consensus as to whether they can directly transfer energy to the dielectric. Therefore we focus on the phonon interfacial transport in this work.

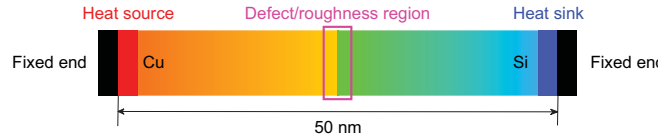

FIG. 1. Illustration of the simulation domain.

II. METHODOLOGY

A schematic of the NEMD computational system is shown in Fig. 1. The structure is periodic in three dimensions and a one-dimensional heat transfer simulation is set up using the LAMMPS package [60], with heat flow perpendicular to the interface. The Cu and Si blocks join through their (100) planes. The Cu block is 72 unit cells long (lattice constant $a = 3.61$ Å) while the Si block is 48 unit cells long ($a = 5.45$ Å), forming a 50-nm-long system with two materials of approximately the same length. The cross-section area of the simulation box, which is parallel to the interface, consists of 12×12 Cu unit cells or 8×8 Si unit cells, so that mismatch is small (Si is 0.6% larger than Cu) to minimize interfacial strain. The 12×12 unit cells in the Cu boundary, which is the layer of unit cells directly adjacent to Si, contain 576 atoms, out of which 288 are in the boundary atomic layer (termed Cu_{L1}). The 8×8 unit cells in the Si boundary contain 512 atoms, out of which 128 are in the boundary atomic layer (termed Si_{L1}). The cross-section dimensions are large enough to eliminate finite size effects, as they are four times the 4×4 Si unit cell area demonstrated to be sufficient by Landry and co-workers [30]. The length dependence of the interfacial thermal transport still exists, but extension to other lengths can readily be made using the linear extrapolation method introduced by Schelling *et al* [61].

Atomic vacancies are created by removing atoms from the boundary atomic layer in either or both materials. We examine both regularly and randomly distributed vacancies. The interfacial vacancy concentration n_v is defined as the ratio of the number of removed atoms to the total number of atoms in the boundary unit cells. For the orderly patterns, we choose three different n_v's, 0.015625 (1/64), 0.03125 (1/32), and 0.0625 (1/16), which allow us to place the initial vacancies evenly in the cross-section atomic plane. For Cu vacancies, $n_v = 1/64$ corresponds to 9 atoms removed from 288 atoms in Cu_{L1} (one vacancy in every 4×4 boundary unit cells, with even spacing, as is shown in Fig. 2). This configuration is termed $Cu_{1/64\text{-reg}}$. Similarly, $n_v = 1/32$ and $n_v = 1/16$ correspond to 18 and 36 atoms removed, respectively (one vacancy in every 4×2 and 2×2 boundary unit cells). For Si vacancies, $n_v = 1/64$ corresponds to 8 atoms removed from 128 atoms in Si_{L1} (one vacancy in every 4×2 boundary unit cells, even spacing, as is shown in Fig. 3). $n_v = 1/32$ and $n_v = 1/16$ correspond to 16 and 32 atoms removed, respectively (one vacancy in every 2×2 and 2×1 boundary unit cells). We find that larger values of n_v will induce dramatic vacancy aggregation to form

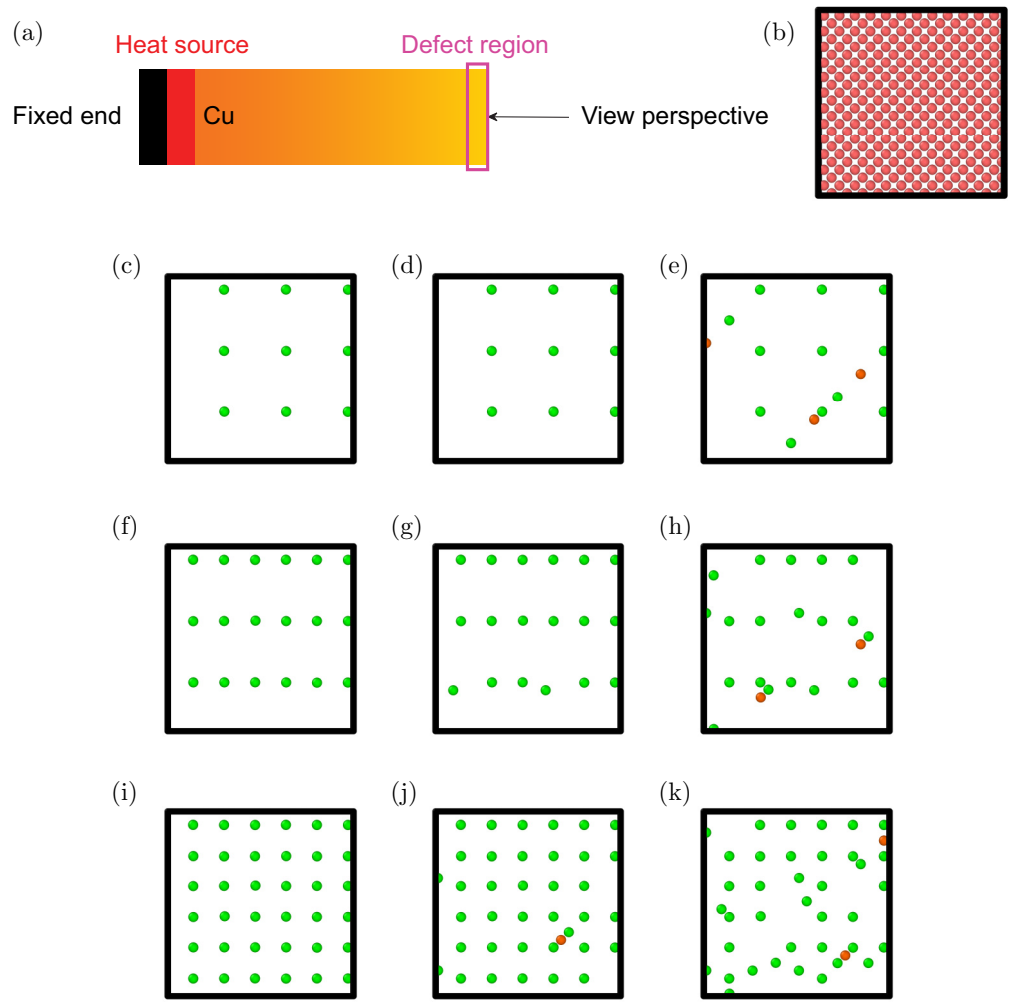

FIG. 2. Visualization of the regularly spaced interfacial point defects in Cu. Green dots represent vacancies and orange dots represent interstitials. (b) The defect-free boundary atomic layer is shown as a reference, where Cu atoms are colored red. Initially ($t = 0$) only vacancies exist, but as the simulation proceeds ($t > 0$) Frenkel defects can be excited during the evolution. (c) $Cu_{1/64\text{-reg}}$, $t = 0$; (d) $Cu_{1/64\text{-reg}}$, 150 K, $t > 0$; (e) $Cu_{1/64\text{-reg}}$, 350 K, $t > 0$; (f) $Cu_{1/32\text{-reg}}$, $t = 0$; (g) $Cu_{1/32\text{-reg}}$, 150 K, $t > 0$; (h) $Cu_{1/32\text{-reg}}$, 350 K, $t > 0$; (i) $Cu_{1/16\text{-reg}}$, $t = 0$; (j) $Cu_{1/16\text{-reg}}$, 150 K, $t > 0$; (k) $Cu_{1/16\text{-reg}}$, 350 K, $t > 0$. It should be noted that for the $Cu_{1/64\text{-reg}}$ case at 150 K vacancies do not move.

voids, resulting in porous materials which we do not consider here. In addition, two special cases of orderly Si defects are shown in Fig. 4, where n_v remains 1/32, but the vacancies are arranged differently. In one of those cases, the defects are in a more concentrated arrangement ($Si_{1/32\text{-conc}}$) with one vacancy in every 4×1 boundary unit cells. In the other special case, the vacancies are arranged in a regular distribution but in the third layer (L3) from the interface instead of the first, which is termed $Si_{1/32\text{-L3}}$. Randomized patterns are done with the same respective n_v's accordingly. The range of n_v in our study is large with respect to typical bulk concentrations in Si and Cu, but vacancies and roughness at an interface can be influenced by manipulating concentrations and temperature in surface growth techniques such as molecular beam epitaxy. In addition, the larger concentration enables determination of trends with a reasonably sized system and feasible computation time.

The modified embedded atomic method (MEAM) potential of Jelinek *et al.* is used for all pairwise and many-body atomic interactions [62]. The bulk Si phonon spectrum, as demonstrated later in this study, is stretched and the cutoff frequency (26 THz) is overpredicted by 10 THz (compared with a cutoff of approximately 16 THz as measured by experiments [63], predicted by simulations using the Tersoff potential [64], and first-principles calculations [65]). This will lead to an overestimated population and thermal conductance of high-frequency Si phonons that must be considered during analysis. The impact of this overestimation is quantified in the results section. Even so, the MEAM potential can reproduce the surface and point-defect formation energies of Cu and Si with excellent accuracy, especially the Cu-Si interaction including point-substitution energy that is missing in other potentials such as the Tersoff. All these are important for modeling interfaces with defects; therefore, we select the MEAM potential.

Initially the system, periodic in all three dimensions, is relaxed in a constant number of atoms, pressure, and temperature (NPT) ensemble for 100 ps under zero pressure at

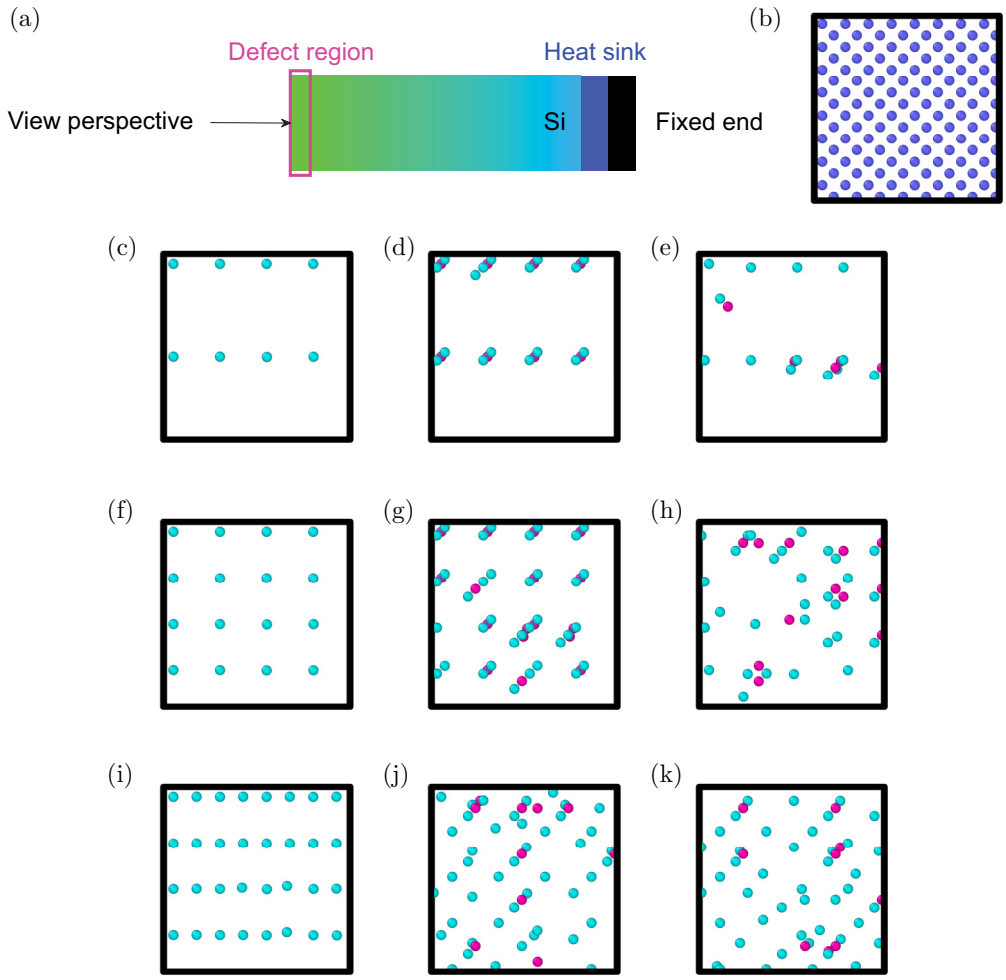

FIG. 3. Visualization of the regularly spaced interfacial point defects in Si. Cyan dots represent vacancies and magenta dots represent interstitials. (b) The defect-free boundary atomic layer is shown as a reference, where Si atoms are colored blue. (c) $Si_{1/64\text{-reg}}$, $t = 0$; (d) $Si_{1/64\text{-reg}}$, 150 K, $t > 0$; (e) $Si_{1/64\text{-reg}}$, 350 K, $t > 0$; (f) $Si_{1/32\text{-reg}}$, $t = 0$; (g) $Si_{1/32\text{-reg}}$, 150 K, $t > 0$; (h) $Si_{1/32\text{-reg}}$, 350 K, $t > 0$; (i) $Si_{1/16\text{-reg}}$, $t = 0$; (j) $Si_{1/16\text{-reg}}$, 150 K, $t > 0$; (k) $Si_{1/16\text{-reg}}$, 350 K, $t > 0$.

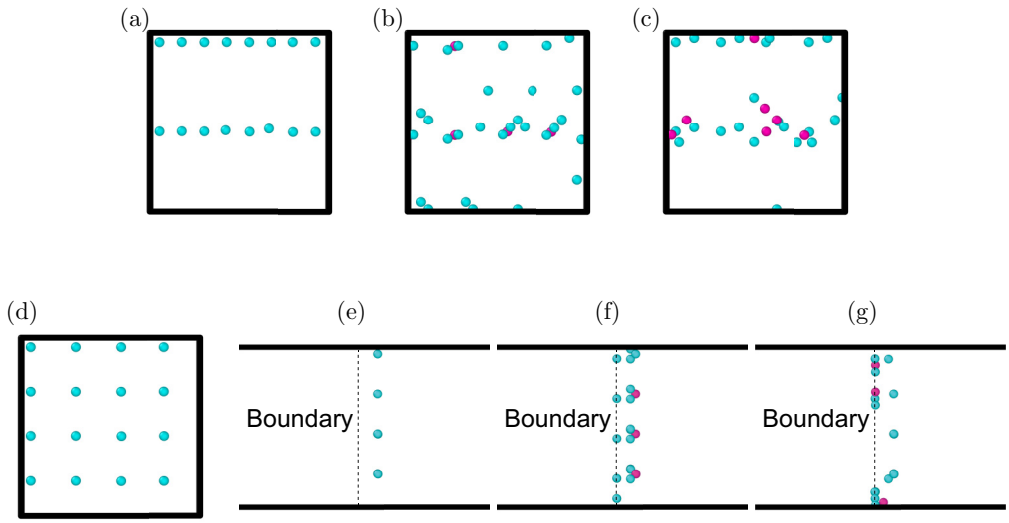

FIG. 4. The two special cases for regular Si interfacial point defects: $Si_{1/32\text{-conc}}$, with (a) $t = 0$, (b) 150 K, $t > 0$, and (c) 350 K, $t > 0$, and $Si_{1/32\text{-L3}}$, with (d) $t = 0$, (e) $t = 0$, (f) 150 K, $t > 0$, and (g) 350 K, $t > 0$.

the initial temperature (150 or 350 K). Then atoms in a region of 10 Å at both ends of the simulation domain are fixed to break periodicity in the heat transfer direction, and heat is inserted into a region of 15 Å adjacent to the fixed end of Cu while it is extracted in a region of the same size next to the fixed end of Si, forming a constant heat flux of 6.7×10^9 W/m^2. It is noteworthy that the heat flux is large in order to generate distinct temperature differences across the interface for more facile analysis, which is consistent with other similar works [58,59]. The simulation then proceeds in a constant number of atoms, volume, and energy (NVE) ensemble for 2 ns to reach steady state. Temperature is averaged and recorded every 10 Å along the heat transfer direction, from which the interfacial thermal transport efficiency is evaluated.

III. RESULTS AND DISCUSSION

A. Defect dynamics: Vacancy migration and creation and annihilation of Frenkel pairs

When conducting molecular dynamics (MD) simulations with defects, it is important to examine the mobility and populations of the defects during the simulation to ensure consistency. By applying Wigner-Seitz cell analysis to the defect region, we visualize the locations of the point defects. Here we present the ordered defect cases in Figs. 2–4, taking advantage of their neat patterns. Before the simulation starts, only vacancies (green for Cu vacancy, cyan for Si vacancy) are present. As the simulation proceeds, three types of activities are observed: migration of the vacancies, and creation and annihilation of Frenkel defects which are vacancy-interstitial pairs caused by the displacement of an atom from its equilibrium position (orange for Cu interstitial, magenta for Si interstitial). The value of $(N_{\text{vacancy}} - N_{\text{interstitial}})$ is conserved, where N refers to the total number of point defects, and therefore n_v during the simulation is constant. Since no more than one vacancy is generated within one boundary unit cell in each material, the vacancies can migrate between different lattice points. The distance of the migration depends on the amplitude of the lattice vibrations, which becomes greater with increasing temperature. In addition, creation and annihilation of Frenkel pairs are observed, especially near Si vacancies (Fig. 3). This is because the Cu atoms are attracted to fill the Si boundary vacancies, since Cu is a "softer" material than Si, namely, bonding in Cu is not as strong or directional as in Si (the cohesive energies are 4.63 eV for Si and 3.54 eV for Cu [62]). In addition, the Si vacancy formation energy is 3.27 eV, which is greater than the sum of Cu vacancy formation energy (1.1 eV) and the formation energy of point substitution with Cu in Si (1.9 eV), indicating that it is favorable to fill Si vacancies with Cu atoms, but not the reverse [62]. At 150 K with $n_v = 1/64$ and $1/32$, the Si Frenkel pairs at multiple vacancy sites are more inclined to be excited simultaneously then annihilate together [Figs. 3(d) and 3(g)]. Some general trends can also be observed: for Cu-vacancy cases, at 150 K vacancies generally stay near their original positions, while they become slightly more active at higher n_v with longer-distance migration and more Frenkel-pair creation [Figs. 2(d), 2(g), and 2(j)]. At 350 K the movements have a greater extent and there are more frequent changes in population, but the original patterns are still visible [Figs. 2(e), 2(h), and 2(k)]. The Si-vacancy cases show the same trends with more dramatic activities. Random vacancies follow the same trends, with fluctuating observations due to the irregular distributions of point defects.

B. Interfacial thermal conductance

The interfacial thermal transport performance is evaluated by the thermal boundary conductance G_{Bd}, which is the inverse of the Kapitza resistance or thermal boundary resistance R_{Bd} [66]:

$$G_{Bd} = \frac{1}{R_{Bd}} = \frac{J}{\Delta T_{Bd}}, \tag{1}$$

where J is the heat flux (unit: W/m^2) and ΔT_{Bd} is the temperature difference at the boundary. Considering that the cases we study have different thicknesses for the defect regions, a uniform effective interfacial thermal conductance G_{int} is defined by directly extrapolating to the interface the linear temperature profiles from the bulk phases, as is shown in Fig. 5(a):

$$G_{\text{int}} = \frac{J}{\Delta T_{\text{int}}}. \tag{2}$$

Consequently ΔT_{int} is measured with the extrapolated temperature profiles, and all impacts from the vacancies are incorporated into G_{int}, which is listed in Table I. For an ideal Cu/Si interface without vacancies, we obtain G_{int}'s of 0.144 GW/m^{2}K at 150 K and 0.193 GW/m^{2}K at 350 K. The results agree with previous reported values from MD by Cruz and co-workers using similar potentials [67] and are consistent with the diffuse mismatch model prediction using the full first-Brillouin zone [68].

The change in G_{int} is represented by ΔG_{int}, which is calculated for each case by comparing G_{int} with that of the ideal interface at the same temperature. Vacancy concentration and distribution are shown to have a great impact on G_{int}. Generally, G_{int} increases with the concentration of Si vacancies by up to 76%, while roughly staying the same for Cu cases. A straightforward explanation, combined with the aforementioned defect dynamics, is that stronger interfacial bonds are induced by the Si vacancies. They can attract Cu atoms to their sites, leading to strong atomic reconstruction in both materials and significant atomic intermixing, but the reverse does not occur. Si atoms do not fill vacancies in Cu, consistent with the higher cohesive energy and vacancy formation energy in Si compared with Cu. Regular vacancy patterns generally induce larger ΔG_{int} than do random vacancies. This can be explained using the results of one of the special Si cases: by comparing $\text{Si}_{1/32\text{-conc}}$ with $\text{Si}_{1/32\text{-reg}}$, it is found that scattered vacancies are better for interfacial thermal transport, as clustered vacancies tend to form local voids which reduce the effective contact area. This explains the lower ΔG_{int} in the random-pattern cases since they include clustered vacancies. If random vacancies are present in both materials, the trend is dominated by that of Si with G_{int} increasing by up to 57.8%. By comparing the $\text{Si}_{1/32\text{-L3}}$ and $\text{Si}_{1/32\text{-reg}}$ cases, we also find that vacancies exactly at the boundary are better for interfacial thermal transport than

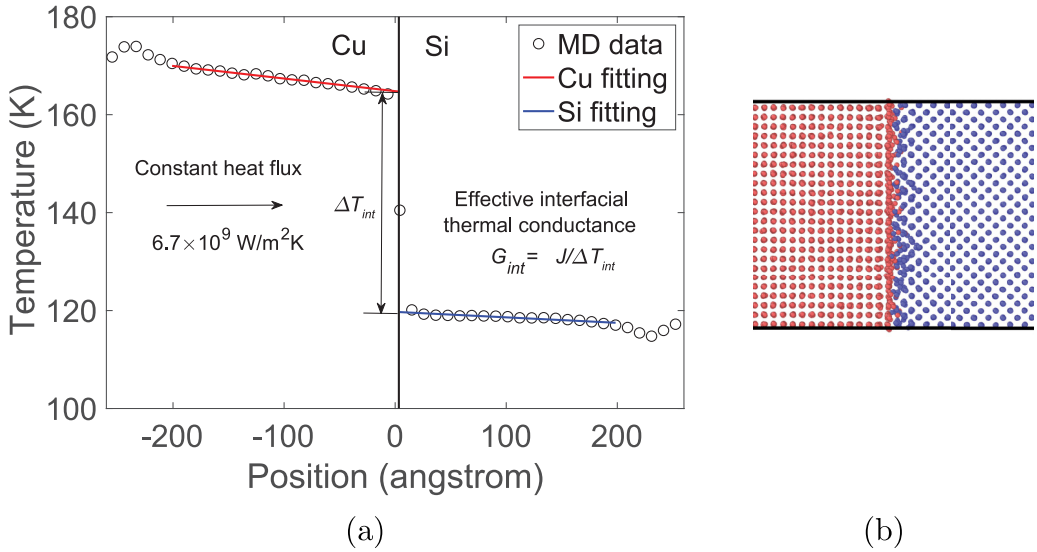

FIG. 5. Temperature profiles and visualization of the Cu/Si interface from the $Si_{1/32\text{-reg}}$ case at 150 K.

those that are not. A straightforward understanding is that Si vacancies even slightly removed from the interface are not able to induce enough interfacial intermixing. Moreover, they will introduce anharmonicity which increases the phonon-scattering rate in the bulk and hinders phonon transport. Still an enhanced G_{int} compared to the ideal interface is observed, because some of the vacancies will migrate to the boundary and partially recover the condition of the $Si_{1/32\text{-reg}}$ case [Fig. 4(f)]. The effect of temperature is also significant, as ΔG_{int} at 150 K is generally 5–50 % lower than that at 350 K for the same initial defect configurations. Here we find a positive correlation between defect dynamics and ΔG_{int}: when the point defects have longer migration paths and more frequent changes in population, as occurs with higher n_v, higher temperature, and Si vacancies rather than Cu vacancies, a larger ΔG_{int} is also observed.

C. Phonon density of states analysis

The phonon frequencies and density of states at the interface can provide insight into the mechanisms of interfacial heat transfer and the basis for the enhancement. Again, it is an advantage of MD simulations that all phonons are expressed, even for irregular structures at an interface. The PDOS is extracted by recording atomic velocities during the simulation and then applying the following autocorrelation technique

TABLE I. The effective G_{int} and PDOS overlap factors S_{ac} and S by Li *et al.* [71]

			150 K				350 K			
	Vacancy concentration		G_{int} (GW/m^{2}K)	ΔG_{int}	S_{ac}	S	G_{int} (GW/m^{2}K)	ΔG_{int}	S_{ac}	S
	Ideal		0.144		0.252	6.05×10^{-14}	0.193		0.245	5.56×10^{-14}
Regular	Cu	1/64	0.145	0.3%	0.265	5.96×10^{-14}	0.194	0.2%	0.239	5.56×10^{-14}
		1/32	0.144	−0.6%	0.254	5.87×10^{-14}	0.195	0.8%	0.287	5.92×10^{-14}
		1/16	0.146	1.3%	0.287	6.20×10^{-14}	0.237	22.5%	0.234	5.33×10^{-14}
	Si	1/64	0.209	44.7%	0.282	5.98×10^{-14}	0.250	29.1%	0.250	5.48×10^{-14}
		1/32	0.253	75.3%	0.274	5.65×10^{-14}	0.340	76.0%	0.288	5.86×10^{-14}
		1/32-conc	0.179	23.6%	0.299	6.16×10^{-14}	0.289	49.6%	0.234	5.12×10^{-14}
		1/32-L3	0.150	3.6%	0.348	6.55×10^{-14}	0.216	11.6%	0.310	5.83×10^{-14}
		1/16	0.223	54.1%	0.288	5.95×10^{-14}	0.318	64.4%	0.294	5.96×10^{-14}
Random	Cu	1/64	0.140	−3.3%	0.273	6.24×10^{-14}	0.196	1.4%	0.236	5.50×10^{-14}
		1/32	0.144	−0.6%	0.290	6.35×10^{-14}	0.189	−2.5%	0.270	5.91×10^{-14}
		1/16	0.146	1.3%	0.327	6.66×10^{-14}	0.188	−2.6%	0.287	5.80×10^{-14}
	Si	1/64	0.152	5.0%	0.334	6.54×10^{-14}	0.220	13.7%	0.262	5.61×10^{-14}
		1/32	0.149	3.3%	0.360	6.54×10^{-14}	0.238	23.2%	0.290	5.82×10^{-14}
		1/16	0.195	35.0%	0.396	6.50×10^{-14}	0.332	71.7%	0.275	5.52×10^{-14}
	Both	1/64	0.154	6.5%	0.332	6.54×10^{-14}	0.204	5.3%	0.302	5.92×10^{-14}
		1/32	0.152	5.1%	0.344	6.56×10^{-14}	0.216	11.6%	0.271	5.76×10^{-14}
		1/16	0.189	30.5%	0.362	6.18×10^{-14}	0.305	57.8%	0.267	5.42×10^{-14}

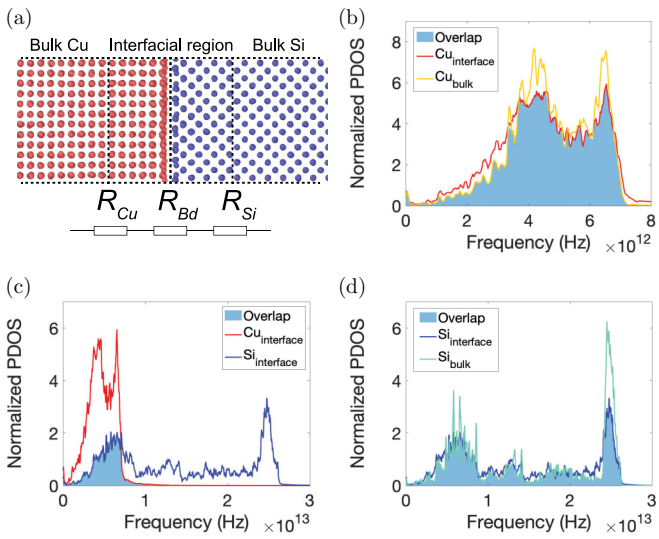

FIG. 6. (a) Illustration of the interfacial regions and "three interfaces" formed between bulk Cu and interfacial Cu, interfacial Cu and interfacial Si, interfacial Si and bulk Si, respectively. The snapshot of the structure is taken from the steady state of the ideal interface at 350 K; note that not all the boundary unit cells in the cross section are shown. The PDOS overlap of the three interfaces, (b) R_{Cu}, (c) R_{int}, and (d) R_{Si}, are shown.

[69,70]:

$$D_{\alpha\beta}(\omega) = \int_0^{\tau} \Gamma_{\alpha\beta}(t)\cos(\omega t)\,dt, \tag{3}$$

where

$$\Gamma_{\alpha\beta}(t) = \frac{\left\langle \sum_{i_{\alpha\beta}=1}^{N_{\alpha\beta}} \mathbf{v}_{i_{\alpha\beta}}(t)\mathbf{v}_{i_{\alpha\beta}}(0)\right\rangle}{\left\langle \sum_{i_{\alpha\beta}=1}^{N_{\alpha\beta}} \mathbf{v}_{i_{\alpha\beta}}(0)\mathbf{v}_{i_{\alpha\beta}}(0)\right\rangle}. \tag{4}$$

Here $D(\omega)$ refers to the PDOS, t is time, ω is phonon angular frequency, i is the atomic index, α is the atom type, β is the region to which the atom belongs, $N_{\alpha\beta}$ is the total number of α atoms in the β region, and $\mathbf{v}$ is the vector velocity of atoms. Equation (3) is done over a period of time τ from the simulation, which is ideally infinity. In our simulation we choose τ to be 50 ps, which equals a time step of 0.125 fs multiplied by 4×10^5 steps.

As demonstrated by previous studies, interfacial thermal conductance strongly depends on the overlap of PDOS from the interfacial regions of the two materials [35,71–73]. The size of these regions is determined by identifying how far from the interface the PDOS exhibits bulk character. In our system the interfacial regions were determined to be three layers of Cu unit cells and two layers of Si unit cells (10.8 Å thick) as shown in Fig. 6(a). In principle there is an additional interface between the bulk and this interfacial region in each material for a total of three interfaces in the system, each with their corresponding thermal resistance (Fig. 6). Fortunately, with a well-defined interfacial region, the resistance between the bulk and this region within a material is typically negligible compared to the thermal boundary resistance R_{Bd} between two materials [73], which is demonstrated by the trivial temperature profile nonlinearity near the interface compared with ΔT_{int} in Fig. 5(a).

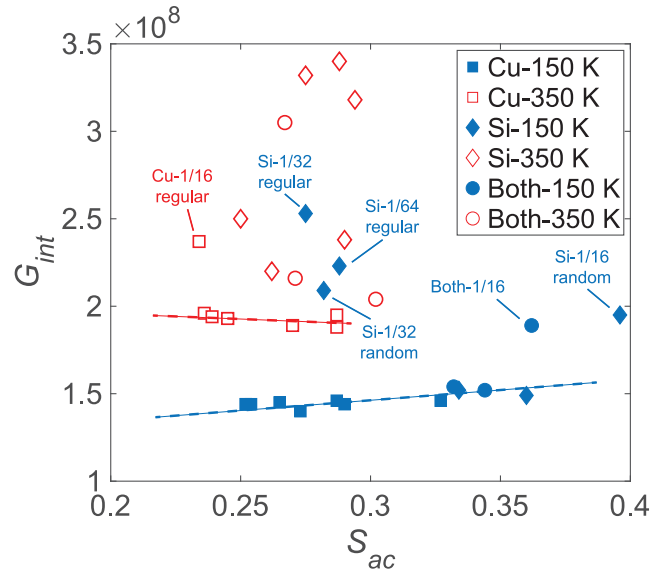

FIG. 7. Relationship between G_{int} and S_{ac}. The 150 K cases (solid symbols) show excellent linear correlation except for several cases where point defects are present in Si. The 350 K cases (open symbols), on the other hand, show poor correlation.

Various methods have been proposed to quantify the overlap [35,71,73]. To facilitate comparisons, we desire an overlap factor that can be normalized to the same scale between zero and 1. Hence we define a new overlap factor S_{ac}, inspired by Li's work and the concept of cross correlation [71]:

$$S_{ac} = \frac{\left|\int_0^{\infty} D_{\alpha}(\omega)D_{\beta}(\omega)\,d\omega\right|^2}{\int_0^{\infty} D_{\alpha}^2(\omega)\,d\omega \int_0^{\infty} D_{\beta}^2(\omega)\,d\omega}. \tag{5}$$

Compared with the original S from Ref. [71],

$$S = \frac{\int_0^{\infty} D_{\alpha}(\omega)D_{\beta}(\omega)\,d\omega}{\int_0^{\infty} D_{\alpha}(\omega)\,d\omega \int_0^{\infty} D_{\beta}(\omega)\,d\omega}, \tag{6}$$

our S_{ac} provides normalized comparisons on a uniform scale. If Eq. (5) is applied to the same material, S_{ac} becomes unity, which represents the largest possible overlap, and the conductance is infinity. The S_{ac}'s of the two interfacial regions for different cases are shown in Fig. 7 and listed in Table I, with the original S also listed for comparison. Generally the two factors predict similar trends, with limited discrepancies at high temperature or large n_v. It is again noteworthy that while the MEAM potential captures the Cu PDOS accurately (cutoff at 7.5 THz for bulk), the Si phonon frequency is overpredicted. Still the Si PDOS is qualitatively correct representing a diamond-structured material, and the trends we learn should still be applicable to mismatched interfaces between materials of face-centered cubic and diamond structures.

D. Elastic and inelastic phonon scattering

As can be seen in Fig. 7, the relationship of G_{int} versus S_{ac} is complex. At 150 K for both orderly and random atomic vacancies G_{int} and S_{ac} align well into a linear relationship. At 350 K, most of the Cu-vacancy cases still align into a linear correlation, with one exception which has a relatively

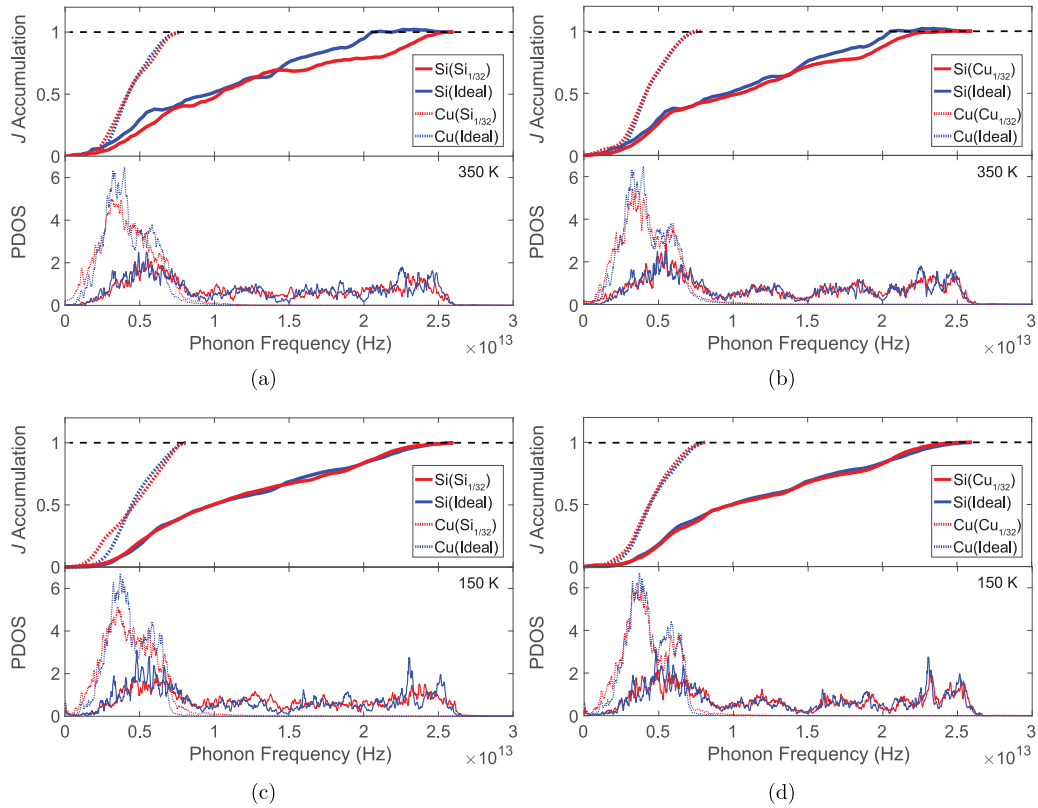

FIG. 8. (a) The normalized spectral heat flux accumulation and corresponding PDOS in the Cu/Si boundary unit cells, comparing the (a) $Si_{1/32\text{-reg}}$ and ideal cases at 350 K, (b) $Cu_{1/32\text{-reg}}$ and ideal cases at 350 K, (c) $Si_{1/32\text{-reg}}$ and ideal cases at 150 K, and (d) $Cu_{1/32\text{-reg}}$ and ideal cases at 150 K.

large n_v of 1/16. These trends are consistent with the findings from previous studies for defects at graphene/boron nitride interfaces [44,45]. Several exceptions to the linear correlation, however, are observed for the Si-vacancy cases. G_{int} for all the Si cases can change significantly even though the overlap of the PDOS remains relatively the same, resulting in a random-appearing scatter. The linear correlation becomes poorer as n_v and temperature increase. Figures 2 and 3 also reveal that only the cases with less defect activities and lattice deformation fall into the linear correlation. Hence it becomes clear that S_{ac} cannot account for the change of G_{int} in all cases. The PDOS overlap, given that it is obtained by correlating PDOS at the same frequencies, constitutes elastic scattering. Hence we postulate that inelastic phonon transport, which becomes more significant at higher temperature and with greater anharmonicity, is important for interfacial thermal transport and causes a majority of the increase in G_{int}.

We first look at the spectral phonon population $n(\omega)$ in the Si boundary unit cells, because Si phonons with a frequency beyond the Cu cutoff must originate from inelastic phonon transport. In classical MD, phonons follow the equipartition of energy distribution, where the total energy for each phonon mode equals k_BT [74]. The occupation of each mode is determined by $\langle n_\lambda \rangle = k_BT/\hbar\omega_\lambda$, where λ denotes the phonon mode, and k_B and $\hbar$ are the Boltzmann and Planck constants, respectively. As a result, $n(\omega)$ at a given temperature is proportional to $D(\omega)/\omega$. If PDOS remains constant, the relative phonon populations at different frequencies become temperature independent: $n(\omega_1)/n(\omega_2) = D(\omega_1)\omega_2/(D(\omega_2)\omega_1)$. This will lead to overprediction of high-frequency phonon populations especially at low temperatures, which, together with the stretched Si phonon spectrum, is discussed later. The PDOS curves are plotted in Fig. 8. Here we divide the Si phonon frequency into four ranges, then all phonons beyond 7.5 THz (Cu cutoff) are from inelastic scattering. Phonons below 7.5 THz can either originate from elastic or inelastic scattering, and for simplicity we label it as "elastic." The values of $n(\omega)$ in Table II are normalized to become fractions of the entire population; thus cases from different temperatures are directly comparable. A comparison between the ideal cases clearly reveals a relatively higher inelastic phonon population at 350 K, which is consistent with previous findings that inelastic scattering becomes more significant at high temperatures [75–79]. The $Si_{1/32\text{-reg}}$ cases have a higher portion of phonon population in the inelastic range than their respective ideal cases at both temperatures, which also applies to the $Cu_{1/32\text{-reg}}$ case at 150 K. This indicates that defects introduce more inelastic phonon scattering at the interface in these three cases, which is mainly manifested by phonons from 7.5 to 13.7 THz. The $Cu_{1/32\text{-reg}}$ case at 350 K, on the other hand, surprisingly shows an increased phonon population below 7.5 THz. A closer look at its PDOS reveals that this is mostly contributed by the increase of phonons below 2.3 THz. Still, the spectral phonon population alone cannot fully explain the enhanced G_{int}, since the interfacial conductance also depends differently

TABLE II. Spectral phonon population of the Si boundary layer. The total n is normalized to unity with arbitrary units.

	Phonon Frequency f (THz)		"Elastic" 0–7.5	Inelastic 7.5–13.7	Inelastic 13.7–19.8	Inelastic 19.8–26
350 K	$\sum n(f)$	Ideal	0.683	0.147	0.080	0.090
			68.3%		31.7%	
		$Si_{1/32\text{-reg}}$	0.660	0.168	0.082	0.090
			66.0%	34.0%		
		$Cu_{1/32\text{-reg}}$	0.758	0.105	0.066	0.072
			75.8%	24.2%		
	$\Delta\sum n(f)$	$Si_{1/32\text{-reg}}$	−3.2%	14.1%	2.1%	0.3%
		$Cu_{1/32\text{-reg}}$	11.1%	−29.1%	−18.5%	−20.9%
150 K	$\sum n(f)$	Ideal	0.762	0.111	0.057	0.070
			76.2%	23.8%		
		$Si_{1/32\text{-reg}}$	0.730	0.134	0.066	0.070
			73.0%	27.0%		
		$Cu_{1/32\text{-reg}}$	0.731	0.137	0.061	0.072
			73.1%	26.9%		
	$\Delta\sum n(f)$	$Si_{1/32\text{-reg}}$	−4.1%	21.0%	15.5%	−1.3%
		$Cu_{1/32\text{-reg}}$	−4.1%	23.4%	6.7%	2.1%

on different phonon modes. Therefore a direct analysis of the spectral heat flux is also necessary.

The interfacial phonon modal heat flux can be quantified based on normal mode decomposition. The MD expression of heat flux (unit W/m^2) is given by

$$J = \left\langle \sum_i (E_i \mathbf{v}_i - \mathbf{S}_i \mathbf{v}_i) \right\rangle \Big/ V, \tag{7}$$

where i refers to the atomic index, E is the total energy (potential and kinetic), $\mathbf{S}$ is the Cauchy stress tensor, and V is the total volume [80–82]. Equation (7) can be extended to calculate the phonon modal heat flux using the time domain direct decomposition method (TDDDM) developed by Zhou *et al.* [83]. First, we need to acquire the atom-projected phonon normal mode amplitude:

$$\Phi_{jl,\mathbf{k},\nu,t} = \left(\frac{m_j}{N}\right)^{0.5} \mathbf{e}^*_{j,\mathbf{k},\nu} \exp(-i\mathbf{k}\mathbf{r}_{jl}) \mathbf{u}_{jl,t}, \tag{8}$$

where ν refers to the phonon branch, $\mathbf{k}$ and $\mathbf{r}$ are the trajectories in the reciprocal and real space, respectively, j and l refer to the jth basis atom in the lth unit cell, m is the atomic mass, N is the total number of unit cells, $\mathbf{u}$ is the vector atomic displacement, t is time, and $\mathbf{e}^*$ is the complex conjugate of the corresponding phonon eigenvector. Equation (8) decomposes atomic displacements into phonon modal contributions and projects them onto the reciprocal space. The reverse transformation of the time derivative of Eq. (8) gives the atomic velocity contributed by each phonon mode:

$$\mathbf{v}_{jl,\mathbf{k},\nu,t} = \frac{1}{(Nm_j)^{0.5}} \mathbf{e}_{j,\mathbf{k},\nu} \exp(i\mathbf{k}\mathbf{r}_{jl}) \dot{\Phi}_{jl,\mathbf{k},\nu,t}. \tag{9}$$

If done correctly, summing Eq. (9) over all the phonon wave vectors and branches should reproduce the atomic velocities. Then by combining Eqs. (7) and (9), the phonon modal heat flux can be expressed as

$$J_{\mathbf{k},\nu} = \sum_{jl} \left\langle \frac{1}{(Nm_j)^{0.5}} [E_{jl,t} \mathbf{e}_{j,\mathbf{k},\nu} \exp(i\mathbf{k}\mathbf{r}_{jl}) \dot{\Phi}_{jl,\mathbf{k},\nu,t} - \mathbf{S}_{jl,t} \mathbf{e}_{j,\mathbf{k},\nu} \exp(i\mathbf{k}\mathbf{r}_{jl}) \dot{\Phi}_{jl,\mathbf{k},\nu,t}] \right\rangle \Big/ V. \tag{10}$$

Similar to Eq. (4), the TDDDM is applied to specific groups of atoms defined in the MD simulation. To best illustrate the interfacial phonon transport, we use the boundary Cu and Si unit cells. Due to the boundary atomic reconstruction and specific interfacial vacancies present in our study, the conventional phonon eigenvectors derived from the bulk phase dynamical matrix do not apply [20,84]. Therefore we treat the entire single layer of boundary Cu (or Si) unit cells as a single supercell, and regard each atom inside the region as a distinct basis atom. Then the dynamical matrix and phonon eigenvectors are calculated at the Γ point, and are then applied in Eq. (10) to calculate $J_{\mathbf{k},\nu}$. It should be noted that our expression of $J_{\mathbf{k},\nu}$ is different from the original equation derived by Zhou and co-workers in Ref. [83]. Instead of using the convoluted normal node amplitude $\Phi_{\mathbf{k},\nu,t}$, we further project it onto each atom as is shown in Eq. (8). This allows us to obtain detailed atomwise heat flux decomposition, which is more suitable for our interfacial regions with broken symmetry. The original expression, which incorporates contributions from all atoms and effectively collapses them into a single unit cell for analysis, is on the other hand a viable option when applied to the bulk phase of materials where all unit cells behave similarly when the observation is averaged over a long time.

Here we present the comparison among three cases, $Si_{1/32\text{-reg}}$, $Cu_{1/32\text{-reg}}$, and the ideal interface, as they are most representative with $Si_{1/32\text{-reg}}$ having the largest ΔG_{int} while $Cu_{1/32\text{-reg}}$ has almost unchanged G_{int} at 350 K. The corresponding cases at 150 K are also shown for reference. For the Cu supercell, there are 558 or 576 atoms in the 12×12 boundary unit cells depending on whether vacancies

TABLE III. Elastic and inelastic contributions to the G_{int}, and their respective increases. The unit of G_{int} is GW/m^{2}K.

	Phonon frequency, f (THz)		"Elastic" 0–7.5	Inelastic 7.5–13.7	Inelastic 13.7–19.8	Inelastic 19.8–26
350 K	$G_{\text{int}}(f)$	Ideal	0.080	0.045	0.056	0.012
			41.6%	58.4%		
		$\text{Si}_{1/32\text{-reg}}$	0.134	0.097	0.038	0.071
			39.4%	60.6%		
		$\text{Cu}_{1/32\text{-reg}}$	0.080	0.047	0.042	0.026
			41.2%	58.8%		
	$\Delta G_{\text{int}}(f)$	$\text{Si}_{1/32\text{-reg}}$	66.7%	119.2%	−32.8%	476.7%
			36.5%	63.5%		
		$\text{Cu}_{1/32\text{-reg}}$	0.1%	6.3%	−26.2%	112.0%
			0.8%	99.2%		
150 K	$G_{\text{int}}(f)$	Ideal	0.055	0.033	0.031	0.025
			38.4%	61.6%		
		$\text{Si}_{1/32\text{-reg}}$	0.096	0.065	0.049	0.043
			37.9%	62.1%		
		$\text{Cu}_{1/32\text{-reg}}$	0.052	0.035	0.031	0.026
			36.1%	63.9%		
	$\Delta G_{\text{int}}(f)$	$\text{Si}_{1/32\text{-reg}}$	72.8%	99.6%	55.3%	74.0%
			37.2%	62.8%		
		$\text{Cu}_{1/32\text{-reg}}$	−6.5%	7.1%	−2.8%	5.4%
			−421.0%	321.0%		

are present or not, resulting in 1674 or 1728 phonon modes sampled at the Γ point. The Si counterpart has 496 or 512 atoms in the 8 × 8 boundary unit cells, equivalent to 1488 or 1536 phonon modes. The calculation of Eq. (10) is done over a simulation time of 12 ns to ensure convergence. It should be noted that atomic movements (Figs. 2–5) near the interface due to structure deformation may potentially undermine the accuracy of normal mode decomposition, which assumes small displacements of atoms from equilibrium positions. However, we average the atomic trajectories over a sufficiently long time, which smooths out the inaccuracies due to occasional large displacements and yields reasonable results. The spectral heat flux accumulation is shown in Fig. 8. It can be seen that for the defected interfaces, the spectral J differs depending on the vacancy distribution and temperature.

Comparing the $\text{Si}_{1/32\text{-reg}}$ case with the ideal interface at 350 K [Fig. 8(a)], it is apparent that the Si spectral heat flux differs significantly; namely, there is an obvious increase in the conduction of high-frequency phonons. Both cases show that Si phonons below 14.3 THz carry 69.5% of the total J, though the detailed spectral distributions are different. At the ideal interface, 99% of the remaining 30.5% heat flux is transferred by phonons from 14.3 to 20.5 THz. However, in the $\text{Si}_{1/32\text{-reg}}$ case phonons in the same frequency range only transfer another 10%, and the remaining 20.5% is carried by phonons above 20.5 THz. In contrast to the Si vacancies, Cu vacancies in the $\text{Cu}_{1/32\text{-reg}}$ case have much less effect on the Si spectral heat flux [Fig. 8(b)]. Even so, at 350 K Si phonons above 20.5 THz carry an additional 8% of the total J with Cu vacancies, indicating the defects' impact is not localized to the material they are intrinsic to. Similarly the Cu spectral heat flux is affected by Si vacancies, which is especially significant at 150 K [Fig. 8(c)]. Overall, the Si spectral heat flux is not as sensitive to Cu interfacial vacancies as it is to Si vacancies. This result is consistent with the observation that the cases with Cu vacancies, despite interfacial restructuring, are still able to keep a distinct interface with minimal atomic intermixing and lattice deformation. For comparison, the corresponding three cases at 150 K are also shown in Figs. 8(c) and 8(d). Generally the impact from defects on Si spectral heat flux becomes much less significant, indicating J scales according to approximately the same ratio.

The conductance from phonons in frequency range $[f_1, f_2]$ can be quantified by calculating its modal accumulation $G_{\text{int}}(f) = \sum_{f_1}^{f_2} G_{\text{int},\mathbf{k},\nu}$. Using the same definition of phonon modal conductance as in Ref. [21], $G_{\text{int},\mathbf{k},\nu}$ is then proportional to modal heat flux: $G_{\text{int},\mathbf{k},\nu} = J_{\mathbf{k},\nu}/\Delta T_{\text{int}}$, where ΔT_{int} is the apparent interfacial temperature jump in MD as illustrated in Fig. 5(a). First we focus on the Si layers at 350 K. The changes in cumulative modal conductance $\Delta G_{\text{int}}(f)$ are shown in Table III. For the $\text{Si}_{1/32\text{-reg}}$ case, $\Delta G_{\text{int}}(f)$ for phonons below 7.5 THz is 66.7% and, if assumed to be elastic, qualitatively agrees with predictions from the atomistic Green's function [36]. Phonons from 7.5 to 13.7 THz show a $\Delta G_{\text{int}}(f)$ of 119.2%, which can be rationally linked to the increase in their relative phonon population. Phonons from 13.7 to 19.8 THz experience a 32.8% decrease in $G_{\text{int}}(f)$, which is also consistent with the reduction in $n(f)$. The greatest $\Delta G_{\text{int}}(f)$ of 476.7% appears for phonons from 19.8 to 26 THz, despite only a 0.3% increase in their relative population. A closer look at their PDOS and spectral heat flux reveals that this is achieved by phonons from 22.8 to 24.3 THz, whose population increases with defects leading to a $G_{\text{int}}(f)$ enhancement from almost 0 to 0.03 GW/m^{2}K. For the $\text{Cu}_{1/32\text{-reg}}$ case, the increase and decrease of $G_{\text{int}}(f)$ follow similar trends, but to a smaller extent. At 150 K, $\Delta G_{\text{int}}(f)$ from each frequency range becomes more similar. Though the $\text{Cu}_{1/32\text{-reg}}$ case is showing alternating increase and decrease for each range, the absolute

change in $G_{\text{int}}(f)$ is very small. The difference in the trends of $\Delta n(f)$ and $\Delta G_{\text{int}}(f)$ can be similarly explained by looking into detailed PDOS changes as mentioned above.

Similarly, we can quantify the elastic versus inelastic conductance contribution and their respective increases, as is listed in Table III. For the $\text{Si}_{1/32\text{-reg}}$ case at 350 K, the elastic ΔG_{int} is about 66.7%, while the inelastic ΔG_{int} is about 82.6%. Overall the elastic and inelastic phonon transport contributes to 36.5% and 63.5% of ΔG_{int}, respectively. The $\text{Cu}_{1/32\text{-reg}}$ case at 350 K shows a slight increase of 0.1% in elastic G_{int}, while inelastic G_{int} increases by 1.7%. Overall the elastic and inelastic phonon transport contributes to 0.8% and 99.2% of ΔG_{int}, respectively. The spectral contributions to G_{int} and ΔG_{int} are similar but to a smaller extent for each case respectively at 150 K, which is consistent with the TDDDM of heat flux across Si/Ge interfaces from NEMD by Feng and co-workers in Ref. [21]. As mentioned above, the equipartition phonon occupation makes the relative spectral phonon population temperature independent. Still the changes in interfacial structure and phonon-scattering phase space [85] with temperature affect PDOS and corresponding modal heat flux. The fact that $G_{\text{int}}(f)$ below 7.5 THz becomes relatively larger at 350 K indicates not all phonons in this range are from elastic transmission; therefore the inelastic $G_{\text{int}}(f)$ could actually be larger than as quantified in Table III. The change in the elastic G_{int} can be explained by the extent of atomic intermixing, which is significant for the $\text{Si}_{1/32\text{-reg}}$ cases and increases phonon transmission [36]. However, for the $\text{Cu}_{1/32\text{-reg}}$ cases minimum intermixing is present and G_{int} is hardly affected.

Both comparisons have shown that interfacial vacancies have more impact on the high-frequency phonons, and, for a Cu/Si interface, inelastic transport's contribution to ΔG_{int} is 1.7 to 110 times larger than its elastic counterpart. Aside from the assumed elastic transmission, it may be argued that the major enhancement in G_{int} is due solely to high-frequency phonons, which coincides with inelastic transport in our case. However, considering that Cu phonons are always within their cutoff frequency, yet Si phonons beyond 7.5 THz increase in both conductance and population (except for the $\text{Cu}_{1/32\text{-reg}}$ case at 350 K), we postulate that inelastic phonon transport is still an important factor as it must support more conversion from lower-frequency Cu phonons to higher-frequency Si phonons. A general implication is that these point defects introduce additional anharmonicity which favors inelastic phonon scattering [86]. Still the actual magnitude of ΔG_{int} depends on the significance of inelastic phonon transport and the consequent high-frequency phonon populations, which are determined by the vacancy distribution and temperature. For example, ΔG_{int} is generally larger at 350 K due to stronger inelastic phonon scattering which appears more frequently at higher temperature. Now we can also reiterate our previous statement of a positive correlation between G_{int} and defect activities: with higher temperature and concentration of boundary vacancies, more lattice deformation and atomic intermixing will be introduced near the interface. The greater anharmonicity and higher temperature both contribute to an increased rate of inelastic phonon transport between the two boundaries. Therefore overall we observe significant increase in G_{int} with higher n_v and temperature, which are also the conditions favoring defect migration and Frenkel pair creation and annihilation.

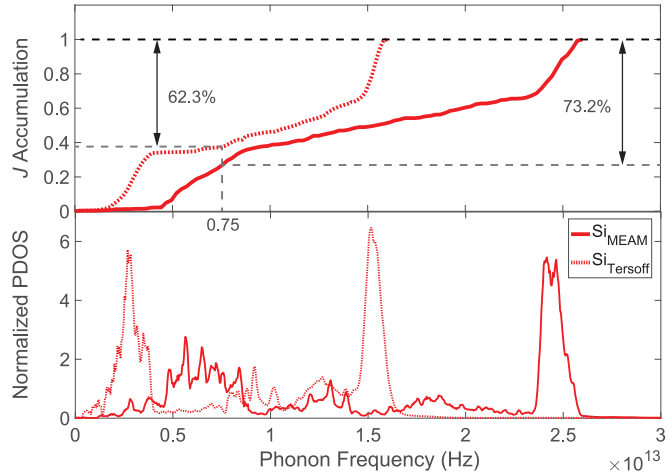

FIG. 9. Comparison of spectral heat flux accumulation and PDOS in bulk Si between MEAM [62] and Tersoff [64] potentials.

When generalizing the simulation results to realistic systems there are several aspects to consider. The equipartition of energy in classical MD results in a phonon distribution of $\langle n_\lambda \rangle = k_B T/\hbar\omega_\lambda$, which deviates from the quantum-mechanical Bose-Einstein distribution $\langle n_\lambda \rangle = 1/(\exp(\hbar\omega_\lambda/k_B T) - 1)$. As mentioned above, this explains the consistent elastic versus inelastic G_{int} regardless of temperature, while in reality inelastic phonon transport should contribute more as temperature increases. In addition, this leads to an overpredicted population of high-frequency phonons, especially at low temperatures. As a result, the inelastic phonon transport is overpredicted. This deviation from reality is further amplified by the MEAM potential that overpredicts Si phonon cutoff frequency by 10 THz, which all contributes to inelastic phonon transport. To gain a quantitative insight of the deviation, Fig. 9 provides comparisons of the spectral heat flux and PDOS in bulk Si using MEAM [62] and Tersoff [64] potentials, the latter of which has been shown to exhibit a phonon cutoff frequency close to experiment. The simulation is conducted at 350 K but results can be extended to 150 K due to the equipartition phonon occupation. It is shown that for phonons above 7.5 THz, the MEAM potential predicts a 17.5% greater contribution to the total heat flux than Tersoff (73.2% compared with 62.3%), which is surprisingly much smaller than the 60% overprediction in phonon cutoff frequency. The spectral heat flux and PDOS at Cu/Si interfaces are different from those in the bulk, but this comparison provides a reasonable estimate of the errors from the MEAM potential for the spectral heat flux and indicates the insights and trends from the simulation results do not change qualitatively.

The error in phonon populations due to the classical equipartition of energy is much smaller than that of the spectral heat flux. As is shown in Table IV, the difference in phonon populations for bulk Si between the classical simulations and the Bose-Einstein distribution is on the order of a few percent. While the difference between MEAM and Tersoff potentials is larger, their respective comparisons with the Bose-Einstein distributions show similar deviations. At

TABLE IV. Relative phonon populations in bulk Si calculated from equipartition and Bose-Einstein distributions using MEAM and Tersoff potentials.

		MEAM		Tersoff	
Phonon frequency f (THz)		0–7.5	above 7.5	0–7.5	above 7.5
Equipartition		57.4%	42.6%	75.4%	24.6%
Bose-Einstein distribution	350 K	60.6%	39.4%	77.5%	22.5%
	150 K	64.9%	35.1%	80.2%	19.8%

350 and 150 K, the MEAM potential overpredicts the phonon population above 7.5 THz by 8.1% and 21.4%, respectively. Based on the observation that the spectral heat flux follows the trend of the PDOS [21], we can expect similar overpredictions in the heat flow. The Tersoff potential shows overpredictions of 9.3% and 24.2%, respectively. This indicates that, regarding inelastic phonon transport, both potentials show similar deviation from reality. Therefore a simple correction to our inelastic G_{int} can be estimated by scaling it down by about 20% (assuming the same deviation at the interfaces) first to match Tersoff potential predictions in the modeling perspective, then further scaling it down by about 10% or 25% depending on the temperature to link to reality. Nonetheless, the trends will be the same. Furthermore, as is mentioned the MEAM-predicted Si PDOS matches those of diamond-structure materials. Therefore the physical significance of our simulations and analyses is still valid and can be generalized to mismatched interfaces between materials of face-centered cubic and diamond structures.

IV. SUMMARY

In this study we identify the effects of interfacial atomic vacancies on thermal conductance across Cu/Si interfaces. Molecular dynamics simulations are performed followed by phonon density of states and normal mode analyses. We find that interfacial vacancies with a concentration below 1/16 generally enhance the interfacial thermal conductance G_{int}, with the largest increase observed being 75.8%. By correlating G_{int} with our newly defined PDOS overlap factor S_{ac}, and conducting phonon normal mode decomposition of the heat flux, we find that high-frequency phonons are more significantly affected by the vacancies. We also confirm that both elastic and inelastic phonon transports need to be considered to explain the change of G_{int}, with the latter contributing to the majority (more than 60%) of ΔG_{int}.

The actual magnitude of ΔG_{int} depends on several factors, which determine the extent of intermixing and significance of inelastic phonon scattering. Higher vacancy concentration n_v tends to cause a larger ΔG_{int} due to greater interfacial intermixing that increases elastic phonon transmission, and greater lattice deformation that leads to more inelastic phonon transport. Vacancies in Si induce higher ΔG_{int} than those in Cu, which can also be explained by the greater interfacial atomic reconstruction they cause. In addition, scattered vacancies enhance G_{int} more than clustered groupings, as they provide more scattering sites for inelastic phonon transport without significantly weakening the interfacial atomic bonds, and vacancies have to be at the boundary atomic layer to form these sites. We also find that ΔG_{int} is generally larger at higher temperature, which is induced by stronger inelastic phonon transport due to greater lattice deformation induced by the point-defect dynamics, and inelastic scattering's own tendency to happen more frequently at high temperature. Therefore a positive correlation can be established between ΔG_{int}, extent of defect migration, and change rate of defect population, as all are favored by higher n_v and temperature.

These trends, derived from controlling the initial positions of the point defects and keeping track of their evolution, may provide new insights into thermal engineering across interfaces. By modifying the material surface roughness at the atomic scale, one can expect to achieve precise control of the interfacial thermal conductance by varying the defect distributions. In addition, vacancy control for Cu is less of a concern during manufacturing than for Si, as G_{int} for Cu stays the same with a 3% interfacial n_v according to our results, while a 2% interfacial n_v in Si can already change G_{int} by more than 20%. One thing to note is that our analyses are made mostly based on the regular-patterned vacancies, while in reality vacancies are more likely to be randomly distributed. However, due to the similar trends they show according to our simulations, the conclusions from orderly defects can be extended to more realistic random cases. We have also suggested a practical way to manipulate inelastic phonon transport at the interface. This will potentially broaden the choices of interfacing materials, because the heat transfer efficiency will no longer be confined by the limited phonon transmission between materials with large lattice mismatch. Still, caution should be taken when projecting simulation predictions to reality considering the limitations of modeling, and certain corrections and compensation should be included. Further studies with more complex and realistic defects are worth investigating.

ACKNOWLEDGMENTS

The authors acknowledge support from the Laboratory Directed Research and Development Program of Pacific Northwest National Laboratory, managed by UT-Battelle, LLC, for the U.S. Department of Energy.

[1] D. G. Cahill, W. K. Ford, K. E. Goodson, G. D. Mahan, A. Majumdar, H. J. Maris, R. Merlin, and S. R. Phillpot, J. Appl. Phys. **93**, 793 (2003).

[2] D. Donadio, Curr. Opin. Green Sustainable Chem. **17** (2019).

[3] J. L. Smoyer and P. M. Norris, Heat Transfer Eng. **40**, 269 (2019).

[4] X. Zhang and L.-D. Zhao, J. Mater. **1**, 92 (2015).
[5] R. Chen, J. Lee, W. Lee, and D. Li, Chem. Rev. **119**, 9260 (2019).
[6] E. Pop, S. Sinha, and K. E. Goodson, Proc. IEEE **94**, 1587 (2006).
[7] D. G. Cahill, P. V. Braun, G. Chen, D. R. Clarke, S. Fan, K. E. Goodson, P. Keblinski, W. P. King, G. D. Mahan, A. Majumdar, H. J. Maris, S. R. Phillpot, E. Pop, and L. Shi, Appl. Phys. Rev. **1**, 011305 (2014).
[8] P. Zhang, P. Yuan, X. Jiang, S. Zhai, J. Zeng, Y. Xian, H. Qin, and D. Yang, Small **14**, 1702769 (2018).
[9] A. Giri and P. E. Hopkins, Adv. Funct. Mater. **30**, 1903857 (2020).
[10] L. Lindsay, C. Hua, X. Ruan, and S. Lee, Mater. Today Phys. **7**, 106 (2018).
[11] T. Ma, P. Chakraborty, X. Guo, L. Cao, and Y. Wang, Int. J. Thermophys. **41**, 9 (2019).
[12] R. Prasher, Proc. IEEE **94**, 1571 (2006).
[13] R. S. Prasher and P. E. Phelan, J. Appl. Phys. **100**, 063538 (2006).
[14] V. B. Mykhaylyk, M. Burt, C. Ursachi, and A. Wagner, Rev. Sci. Instrum. **83**, 034902 (2012).
[15] R. Dhuley, Cryogenics **101**, 111 (2019).
[16] K. Gordiz and A. Henry, J. Appl. Phys. **119**, 015101 (2016).
[17] B. Latour, N. Shulumba, and A. J. Minnich, Phys. Rev. B **96**, 104310 (2017).
[18] Z. Liang and M. Hu, J. Appl. Phys. **123**, 191101 (2018).
[19] T. Zhan, S. Minamoto, Y. Xu, Y. Tanaka, and Y. Kagawa, AIP Adv. **5**, 047102 (2015).
[20] K. Gordiz and A. Henry, Sci. Rep. **6**, 23139 (2016).
[21] T. Feng, Y. Zhong, J. Shi, and X. Ruan, Phys. Rev. B **99**, 045301 (2019).
[22] A. Ward and D. A. Broido, Phys. Rev. B **77**, 245328 (2008).
[23] K. Sääskilahti, J. Oksanen, J. Tulkki, and S. Volz, Phys. Rev. B **90**, 134312 (2014).
[24] M. Shen, W. J. Evans, D. Cahill, and P. Keblinski, Phys. Rev. B **84**, 195432 (2011).
[25] J. C. Duda, T. S. English, E. S. Piekos, W. A. Soffa, L. V. Zhigilei, and P. E. Hopkins, Phys. Rev. B **84**, 193301 (2011).
[26] C. B. Saltonstall, C. A. Polanco, J. C. Duda, A. W. Ghosh, P. M. Norris, and P. E. Hopkins, J. Appl. Phys. **113**, 013516 (2013).
[27] X. W. Zhou, R. E. Jones, J. C. Duda, and P. E. Hopkins, Phys. Chem. Chem. Phys. **15**, 11078 (2013).
[28] R. J. Stevens, L. V. Zhigilei, and P. M. Norris, Int. J. Heat Mass Transf. **50**, 3977 (2007).
[29] P. E. Hopkins, T. Beechem, J. C. Duda, K. Hattar, J. F. Ihlefeld, M. A. Rodriguez, and E. S. Piekos, Phys. Rev. B **84**, 125408 (2011).
[30] E. S. Landry and A. J. H. McGaughey, Phys. Rev. B **79**, 075316 (2009).
[31] P. E. Hopkins, J. C. Duda, C. W. Petz, and J. A. Floro, Phys. Rev. B **84**, 035438 (2011).
[32] J. C. Duda and P. E. Hopkins, Appl. Phys. Lett. **100**, 111602 (2012).
[33] Z. Liang and P. Keblinski, Phys. Rev. B **90**, 075411 (2014).
[34] K. Gordiz and A. Henry, J. Appl. Phys. **121**, 025102 (2017).
[35] T. S. English, J. C. Duda, J. L. Smoyer, D. A. Jordan, P. M. Norris, and L. V. Zhigilei, Phys. Rev. B **85**, 035438 (2012).
[36] Z. Tian, K. Esfarjani, and G. Chen, Phys. Rev. B **86**, 235304 (2012).
[37] L. Jia, S. Ju, X. Liang, and X. Zhang, Mater. Res. Express **3**, 095024 (2016).
[38] W. Ih Choi, K. Kim, and S. Narumanchi, J. Appl. Phys. **112**, 054305 (2012).
[39] B. Gotsmann and M. A. Lantz, Nat. Mater. **12**, 59 (2012).
[40] Y. Zhang, D. Ma, Y. Zang, X. Wang, and N. Yang, Front. Energy Res. **6**, 48 (2018).
[41] P. E. Hopkins, ISRN Mech. Eng. **2013**, 682586 (2013).
[42] C. T. Walker and R. O. Pohl, Phys. Rev. **131**, 1433 (1963).
[43] T. Feng, X. Ruan, Z. Ye, and B. Cao, Phys. Rev. B **91**, 224301 (2015).
[44] X. Liu, G. Zhang, and Y.-W. Zhang, Nano Lett. **16**, 4954 (2016).
[45] M. Li, B. Zheng, K. Duan, Y. Zhang, Z. Huang, and H. Zhou, J. Phys. Chem. C **122**, 14945 (2018).
[46] B. Smith, L. Lindsay, J. Kim, E. Ou, R. Huang, and L. Shi, Appl. Phys. Lett. **114**, 221902 (2019).
[47] P. E. Hopkins, L. M. Phinney, J. R. Serrano, and T. E. Beechem, Phys. Rev. B **82**, 085307 (2010).
[48] E. A. Scott, K. Hattar, C. M. Rost, J. T. Gaskins, M. Fazli, C. Ganski, C. Li, T. Bai, Y. Wang, K. Esfarjani, M. Goorsky, and P. E. Hopkins, Phys. Rev. Mater. **2**, 095001 (2018).
[49] A. Giri, S. W. King, W. A. Lanford, A. B. Mei, D. Merrill, L. Li, R. Oviedo, J. Richards, D. H. Olson, J. L. Braun, J. T. Gaskins, F. Deangelis, A. Henry, and P. E. Hopkins, Adv. Mater. **30**, 1804097 (2018).
[50] C. S. Gorham, K. Hattar, R. Cheaito, J. C. Duda, J. T. Gaskins, T. E. Beechem, J. F. Ihlefeld, L. B. Biedermann, E. S. Piekos, D. L. Medlin, and P. E. Hopkins, Phys. Rev. B **90**, 024301 (2014).
[51] P. G. Klemens, Proc. Phys. Soc. London Sect. A **68**, 1113 (1955).
[52] P. K. Schelling, S. R. Phillpot, and P. Keblinski, J. Appl. Phys. **95**, 6082 (2004).
[53] T. Watanabe, B. Ni, S. R. Phillpot, P. K. Schelling, and P. Keblinski, J. Appl. Phys. **102**, 063503 (2007).
[54] C. Kimmer, S. Aubry, A. Skye, and P. K. Schelling, Phys. Rev. B **75**, 144105 (2007).
[55] Y. Mao, D. Hu, C. Wu, Q. Liu, and Y. Xiong, Mater. Res. Express **6**, 116531 (2019).
[56] E. S. Landry and A. J. H. McGaughey, Phys. Rev. B **80**, 165304 (2009).
[57] J. E. Turney, A. J. H. McGaughey, and C. H. Amon, Phys. Rev. B **79**, 224305 (2009).
[58] Y. Wang, X. Ruan, and A. K. Roy, Phys. Rev. B **85**, 205311 (2012).
[59] Z. Lu, Y. Wang, and X. Ruan, Phys. Rev. B **93**, 064302 (2016).
[60] S. Plimpton, J. Comput. Phys. **117**, 1 (1995).
[61] P. K. Schelling, S. R. Phillpot, and P. Keblinski, Phys. Rev. B **65**, 144306 (2002).
[62] B. Jelinek, S. Groh, M. F. Horstemeyer, J. Houze, S. G. Kim, G. J. Wagner, A. Moitra, and M. I. Baskes, Phys. Rev. B **85**, 245102 (2012).
[63] J. Kulda, D. Strauch, P. Pavone, and Y. Ishii, Phys. Rev. B **50**, 13347 (1994).
[64] J. Tersoff, Phys. Rev. B **37**, 6991 (1988).
[65] S. Wei and M. Y. Chou, Phys. Rev. B **50**, 2221 (1994).
[66] G. L. Pollack, Rev. Mod. Phys. **41**, 48 (1969).
[67] C. Abs da Cruz, P. Chantrenne, R. Gomes de Aguiar Veiga, M. Perez, and X. Kleber, J. Appl. Phys. **113**, 023710 (2013).

[68] P. Reddy, K. Castelino, and A. Majumdar, Appl. Phys. Lett. **87**, 211908 (2005).
[69] J. M. Dickey and A. Paskin, Phys. Rev. **188**, 1407 (1969).
[70] H. Bao, X. L. Ruan, and M. Kaviany, Phys. Rev. B **78**, 125417 (2008).
[71] B. Li, J. H. Lan, and L. Wang, Phys. Rev. Lett. **95**, 104302 (2005).
[72] S. Shin, M. Kaviany, T. Desai, and R. Bonner, Phys. Rev. B **82**, 081302(R) (2010).
[73] J. Shi, Y. Dong, T. Fisher, and X. Ruan, J. Appl. Phys. **118**, 044302 (2015).
[74] M. Puligheddu, Y. Xia, M. Chan, and G. Galli, Phys. Rev. Mater. **3**, 085401 (2019).
[75] T. Feng, L. Lindsay, and X. Ruan, Phys. Rev. B **96**, 161201(R) (2017).
[76] T. Feng and X. Ruan, Phys. Rev. B **93**, 045202 (2016).
[77] J. S. Kang, M. Li, H. Wu, H. Nguyen, and Y. Hu, Science **361**, 575 (2018).
[78] S. Li, Q. Zheng, Y. Lv, X. Liu, X. Wang, P. Y. Huang, D. G. Cahill, and B. Lv, Science **361**, 579 (2018).
[79] F. Tian, B. Song, X. Chen, N. K. Ravichandran, Y. Lv, K. Chen, S. Sullivan, J. Kim, Y. Zhou, T.-H. Liu, M. Goni, Z. Ding, J. Sun, G. A. G. Udalamatta Gamage, H. Sun, H. Ziyaee, S. Huyan, L. Deng, J. Zhou, A. J. Schmidt, S. Chen, C.-W. Chu, P. Y. Huang, D. Broido, L. Shi, G. Chen, and Z. Ren, Science **361**, 582 (2018).
[80] J. H. Irving and J. G. Kirkwood, J. Chem. Phys. **18**, 817 (1950).
[81] T. Ohara, J. Chem. Phys. **111**, 9667 (1999).
[82] D. Torii, T. Nakano, and T. Ohara, J. Chem. Phys. **128**, 044504 (2008).
[83] Y. Zhou, X. Zhang, and M. Hu, Phys. Rev. B **92**, 195204 (2015).
[84] K. Gordiz and A. Henry, New J. Phys. **17**, 103002 (2015).
[85] L. Lindsay and D. A. Broido, J. Phys.: Condens. Matter **20**, 165209 (2008).
[86] N. Q. Le, C. A. Polanco, R. Rastgarkafshgarkolaei, J. Zhang, A. W. Ghosh, and P. M. Norris, Phys. Rev. B **95**, 245417 (2017).